



Enhanced reductive degradation of tetrabromobisphenol A by biochar supported sulfidated nanoscale zero-valent iron: Selectivity and core reactivity

Feilong Gao^a, Honghong Lyu^{b,*}, Shakeel Ahmad^a, Siyu Xu^a, Jingchun Tang^{a,*}

^a MOE Key Laboratory of Pollution Processes and Environmental Criteria/Tianjin Engineering Center of Environmental Diagnosis and Contamination Remediation, College of Environmental Science and Engineering, Nankai University, Tianjin 300350, China

^b Tianjin Key Laboratory of Clean Energy and Pollution Control, School of Energy and Environmental Engineering, Hebei University of Technology, Tianjin 300401, China

ARTICLE INFO

Keywords:

S-nZVI/BC

Core-shell

TBBPA

Direct electron transfer

Core properties

ABSTRACT

A core-shell structure of sulfidated nanoscale zero-valent iron deposited on biochar (S-nZVI/BC) was synthesized and the performance of S-nZVI/BC on tetrabromobisphenol A (TBBPA) degradation was investigated. Detailed characterizations indicated that controlling S content altered distribution of S species (i.e., S^{2-} , S_2^{2-} , and S_n^{2-}) in shell and core and achieved higher hydrophobicity and lower electron-transfer resistance. S-nZVI/BC was highly reactive (~ 4.3 – 11.3 times) and selective (~ 78.9 – 152.6 times) over nZVI/BC for TBBPA degradation. Besides, BC improved reactivity and selectivity of S-nZVI by 0.17 and 1.35 times, respectively, deriving from increased electron-transfer, enhanced hydrophobicity, and more surface reduced S species. Thus, sulfidation and BC enhanced reactivity and selectivity of S-nZVI/BC by combining respective merits. Effects of initial TBBPA concentration, pH, and particles dosage on TBBPA degradation by S-nZVI/BC were also investigated. Remarkably, mechanism investigation revealed that core properties instead of shell dominated reactivity and TBBPA debromination mainly involved direct electron-transfer rather than atomic H.

1. Introduction

Nanoscale zero-valent iron (nZVI) is one of the most promising approaches for the remediation of halogenated organic compound (HOC)-contaminated groundwater in anaerobic conditions [1–4]. However, the rapid aggregation and indiscriminate reaction (i.e., the hydrogen evolution reaction (HER)) of nZVI reduce its mobility, reactivity, and selectivity, further limiting its large-scale implementation for in situ remediation [5,6]. Traditionally, polymer stabilization, noble metal doping, loading on a support, and sulfidation treatment are the most promising ones to improve the effectiveness of nZVI [7–10]. Whereas, sulfidation of nZVI is an important measure to optimize particles for field remediation performance in recent years [2,11,12]. Growing interest in sulfidation technology stems from enhancing effect on selectivity remarkably [13–16]. Impressively, the direct electron transfer has been widely demonstrated to mediate dehalogenation reaction (e-mediated) [14,17], while a few studies have shown that atomic H is generated and accumulates on S-nZVI surface to mediate the

dehalogenation reaction (H-mediated) [18,19]. The contradictory observations suggest that the e-mediated and H-mediated mechanisms might work in synergy and distinct dominant mechanisms might be applicable to different contaminants according to their structure, reduction potential and hydrophobicity [2]. Thus, the difference in reactivity induced by sulfidation is compound-specific and likely depends on the properties of the target contaminants/functional groups (e.g., -Br, -NO₂) [20]. Moreover, the relative importance of atomic H and direct electron transfer on contaminants degradation needs to be further clarified. Since the reaction of HOCs with nZVI-based materials is a surface-mediated reaction, the performance can be improved by designing the surface properties of nZVI [21,22]. The S-nZVI_{co} method (i.e., dropwise addition of a NaBH₄ and Na₂S₂O₄ solution into an aqueous suspension containing dissolved Fe²⁺ or Fe³⁺ ions) was a common way to synthesize sulfidated nZVI. Notably, recent works have suggested that the surface information (e.g., S speciation/content) of S-nZVI_{co} correlates well with the reactivity and selectivity [23,24]. Likewise, the S speciation/content in the core has also been

* Corresponding authors.

E-mail addresses: honghonglyu@hebut.edu.cn (H. Lyu), tangjch@nankai.edu.cn (J. Tang).

<https://doi.org/10.1016/j.apcatb.2022.122246>

Received 19 September 2022; Received in revised form 16 November 2022; Accepted 30 November 2022

Available online 2 December 2022

0926-3373/© 2022 Elsevier B.V. All rights reserved.

demonstrated to play an active role on performance of S-nZVI_{co} in addition to surface properties [25,26]. Therefore, both surface and core properties might be responsible for the enhanced contaminant transformation. However, till now, the relative significance of surface properties versus core properties on reactivity in S-nZVI_{co} has not been reported and remains unknown.

Impressively, loading technology has been proven to aid in the stabilization and dispersion of engineered nanoparticles [9,27]. However, biochar (BC) is a common carrier material, which can protect and distribute nanoparticles to avoid their defects (e.g., poor stability in air and strong aggregation tendency) to a greater extent and achieve pre-enrichment of contaminants [28,29]. For instance, Mackenzie et al. reported that carbon-iron particles improved the reactivity by enhancing TCE concentrations on the nZVI surface [30]. Besides, unlike nanoparticles without support, BC carrier with a lower particle size (0.5–2 µm) (e.g., carbon colloids) improves mobility of nanoparticles in porous media by electrostatic repulsion between the colloid and sediment surfaces [31,32]. BC can improve electron transfer by suppressing the formation of oxide layer on the particle surface [33]. Meanwhile, BC also increases the availability of nZVI by promoting its dispersion, resulting in more electrons being transferred to the contaminants [34,35]. Consequently, the couple of sulfidation and BC (S-nZVI/BC) is expected to be the most feasible approach for enhancing reactivity and selectivity of nZVI toward contaminants. However, the impact of BC on performance of S-nZVI in contaminants transformation remains to be elucidated.

In sum, the S-nZVI/BC with different amounts of S were synthesized and characterized systematically to determine how the physicochemical properties (morphology, crystalline structure, S speciation/content, hydrophobicity, and electron transfer-resistance) affected the reactivity and selectivity of S-nZVI/BC with TBBPA (model contaminant) in anaerobic condition. The promoting effects of coupling sulfidation and BC were comprehensively investigated to address the broad perspective of reductive removal of contaminants by S-nZVI/BC, and to find out whether e-mediated or H-mediated mechanism dominated TBBPA debromination by TBA quenching experiments and comparison experiment with D₂O instead of H₂O as reaction medium. Besides, the effects of initial TBBPA concentration, S-nZVI/BC dose, and initial solution pH on TBBPA degradation by S-nZVI/BC also were determined.

2. Experimental section

2.1. Chemical reagents

Details regarding the chemicals used are provided in the [supporting information](#) (Text S1).

2.2. Synthesis of S-nZVI/BC and S-nZVI

BC was prepared using corn stalk as the raw material. Detailed preparation process is described in the [supporting information](#) (Text S2). The S-nZVI/BC was synthesized by the S-nZVI_{co} method according to previously reported methods [31,36]. Briefly, a homogeneously dispersed phase of 200 mL aqueous solution containing Fe²⁺ (2.014 g L⁻¹) and BC (0.7875 g L⁻¹) was obtained by ultrasonication of the suspension. Subsequently, a 200 mL mixed solution containing NaBH₄ (6.8332 g L⁻¹) and Na₂S₂O₄ (0.9375 g L⁻¹) was added dropwise (~5 mL min⁻¹) to generate particle with an theoretical S/Fe molar ratio ([S/Fe]_{dose}) of 0.3 and an S-nZVI/BC mass ratio of 3 under N₂ purging. S-nZVI/BC with different [S/Fe]_{dose} (0, 0.1, 0.2, 0.3, 0.4, and 0.5) were synthesized using the same procedure by changing the concentration of Na₂S₂O₄. Specifically, nZVI/BC corresponded to S-nZVI/BC ([S/Fe]_{dose}=0). S-nZVI ([S/Fe]_{dose}=0.3) was synthesized using the same procedure, except for without addition of BC. The NaBH₄/Fe molar ratio was 5 during the synthesis of all materials. The as-synthesized suspensions were filtered and washed with ethanol/water three times and

lyophilized. The resulting particles were stored in a sealed vial for use. Novelty, the actual S/Fe molar ratio ([S/Fe]_{particles}) in bulk particles was determined by ICP-OES. Herein, the S-nZVI/BC ([S/Fe]_{dose}=0.1), S-nZVI/BC ([S/Fe]_{dose}=0.2), S-nZVI/BC ([S/Fe]_{dose}=0.3), S-nZVI ([S/Fe]_{dose}=0.3), S-nZVI/BC ([S/Fe]_{dose}=0.4), and S-nZVI/BC ([S/Fe]_{dose}=0.5) were named using actual S/Fe molar ratio as S-nZVI/BC (0.035), S-nZVI/BC (0.059), S-nZVI/BC (0.090), S-nZVI (0.082), S-nZVI/BC (0.105), and S-nZVI/BC (0.126), respectively. Unless otherwise specified, the 0.035, 0.059, 0.090, 0.082, 0.105, and 0.126 in parentheses represented the actual S/Fe molar ratio ([S/Fe]_{particles}) of particles.

2.3. Batch experiments

Batch TBBPA degradation experiments were conducted in 60 mL screw-capped glass bottles with PTFE-lined silicone septa containing 40 mL of an aqueous suspension of 2 g L⁻¹ S-nZVI/BC with different [S/Fe]_{particles} or S-nZVI and 10 mg L⁻¹ TBBPA under anoxic conditions. The reaction was initiated by adding 0.4 mL TBBPA stock solution (1000 mg L⁻¹, deoxygenated methanol) into a 39.6 mL suspension. Then, the reactor bottles were sealed immediately and shaken on an end-over-end rotator (250 rpm) at 25 °C in the dark. The methanol (cosolvent) content in the reaction solution (methanol/water mixture) was only 1% (v/v), lower than that in previous studies where a water/cosolvent mixture was composed of 2, 40, or 50% cosolvent (v/v) [37–40], thus minimizing the effect of the cosolvent on TBBPA transformation. Control experiment was conducted in parallel without the addition of particles. All reaction systems were sacrificially sampled at predetermined times (i.e., 1, 2, 4, 6, 9, 12, and 24 h), and then magnetic separation was carried out to analyze the TBBPA and its transformation products in solid and liquid phases respectively. After separation, the material was dried and then weighed. The material loss rate was below 1% (negligible). For the concentrations of TBBPA and its transformation products in the liquid phase, a 0.5 mL aliquot was taken from each liquid and thoroughly mixed with 0.5 mL methanol to make sure the complete dissolution of TBBPA and its transformation products [38]. Specially, a cosolvent of 1% methanol (v/v) was used in the reaction system, while a cosolvent of 50% methanol (v/v) was used in the HPLC analysis system for analyzing the concentrations of TBBPA and its transformation products in the liquid phase. Then, a 0.5 mL aliquot was collected from the solution above for HPLC analysis. In addition, TBBPA and its transformation products on the solid phase were recovered through ultrasonic extraction (20 min) using 10 mL methanol three times consecutively. The supernatants were combined, and a 0.5 mL aliquot was collected for subsequent HPLC analysis. All experiments were carried out in triplicate.

Additionally, to further explore the performance of S-nZVI/BC in TBBPA transformation, various experimental setups were conducted to investigate the influence of different variables, such as the S-nZVI/BC dosage (1, 1.5, and 2 g L⁻¹), initial TBBPA concentration (5, 10, and 20 mg L⁻¹), and initial pH (3.0–11.0), on TBBPA degradation by S-nZVI/BC (0.090). Notably, the initial average recovery rate of TBBPA was 93.5% at different pH, which met the experimental demand. Specific details were provided in [Table S1](#). In addition, different concentrations (1–200 mM) of TBA, a scavenger for atomic H, were added to study the role of atomic H in TBBPA degradation by S-nZVI/BC (0.090) [41]. Meanwhile, when other reaction conditions remain unchanged, the comparison experiment with D₂O instead of H₂O as reaction medium was conducted to further verify the role of atomic H.

2.4. Analytical methods

The analyses of TBBPA and its four transformation products (tri-BBPA, di-BBPA, mono-BBPA, and BPA) were performed by high-performance liquid chromatography (HPLC, Agilent 1260 Infinity), as shown in the [supporting information](#) (Text S3). In order to get a more

reliable quantitative analysis of TBBPA and its four transformation products, the respective standard curves were plotted and their R^2 values were greater than 0.999. The summed molar concentrations of TBBPA and its four transformation products (tri-BBPA, di-BBPA, mono-BBPA, and BPA) ranged from 90% to 105% of the initial TBBPA concentration in the respective batch experiments, which suggested no formation of other transformation products. The actual S/Fe molar ratio ($[S/Fe]_{\text{particles}}$) in bulk particles was determined by inductively coupled plasma-optical emission spectroscopy (ICP-OES, Agilent 5110) after the particle was digested using aqua regia solution [28]. The limitation of ICP-OES is 0.1 mg L^{-1} , which met the requirements of the test in this experiment. Details of the ICP-OES analysis and measurements are provided in Table S2. Aqueous Br ions were determined by ion chromatography (IC, PerkinElmer ELAN DRC-e). A contact angle goniometer (Dataphysics OCA40) was used to measure the water contact angles of particles to determine their relative hydrophobicity. Cyclic voltammetry (CV) and electrochemical impedance spectroscopy (EIS) were applied to analyze the electrochemical properties of particles by an electrochemical work station (CorrTest CS310H), as described previously [42]. The Fe^0 content was calculated by measuring the generated H_2 after acidification of $\sim 30 \text{ mg}$ of each particle by 10 mL of 37% HCl [26]. After reaction, the H_2 in the headspace was quantified by an Agilent 7890 A GC-TCD system [23].

Details of the particle characterization are described in the supporting information (Text S4). Notably, the Fe and S species on the surface were mainly explored by XPS without ion sputtering (depth profiling), which detects their states primarily on the surface ($<10 \text{ nm}$) [43]. However, XPS combined with ion sputtering (depth profiling) was used to analyze the Fe and S species in the core of particles ($>10 \text{ nm}$) [20,26]. Therefore, to distinguish the influences of the core and shell on the reactivity, the surface ($<10 \text{ nm}$ depth) was defined as the shell of particles, and the inner zone (deeper than $\sim 10 \text{ nm}$) was defined as the core of particles.

The main focus of this research was to achieve degradation rather than simply remove TBBPA by particles, so the degradation efficiency (DE_{TBBPA}) was defined (Eq. (1)). In addition, the degradation rates of TBBPA by S-nZVI/BC and nZVI/BC followed pseudo-first-order kinetics models. The surface-area-normalized degradation rate constant was calculated (Eqs. (2) and (3)):

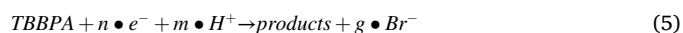
$$DE_{\text{TBBPA}} = \frac{C_0 - C}{C_0} \times 100\% \quad (1)$$

$$k_{\text{obs,TBBPA}} = -\frac{\ln(C_{t,\text{TBBPA}}/C_{0,\text{TBBPA}})}{t} \quad (2)$$

$$k_{\text{SA,TBBPA}} = \frac{k_{\text{obs,TBBPA}}}{a_s \times \rho_m} \quad (3)$$

where C_0 (mg L^{-1}) is the initial concentration of TBBPA at time 0 (h) in the liquid phase; C (mg L^{-1}) is the sum concentration of TBBPA in the liquid and solid phases at time t (h); a_s and ρ_m are the specific surface area ($\text{m}^2 \text{ g}^{-1}$) and concentration (g L^{-1}) of particles, respectively; and $k_{\text{obs,TBBPA}}$ (h^{-1}) and $k_{\text{SA,TBBPA}}$ ($\text{L m}^{-2} \text{ h}^{-1}$) stand for the degradation rate constant and surface-area-normalized degradation rate constant of TBBPA, respectively.

Herein, the electron efficiency (EE) of particles for TBBPA degradation was also evaluated based on the composition of the total reaction products (i.e., H_2 and TBBPA degradation products) [6]. The molar concentration (MC) (mmol L^{-1}) and molar quantity (MQ) (mmol) of TBBPA and its transformation products after 24 h reaction were shown in Table S3. Here, the electron efficiency represented selectivity, which was the fraction of electron equivalents from Fe^0 that was used by reduction of TBBPA (to all products). Furthermore, to quantify ϵ_e and EE, the following half reactions were assumed (Eqs. (4) and (5)):



The values of n , m and g depend on the products formed. For the major products observed in this study, n is 2, 4, 6, and 8 for tri-BBPA, di-BBPA, mono-BBPA, and BPA, respectively.

The EE was calculated (Eq. (6)):

$$EE = \frac{\sum_i n_i p_i}{\sum_i n_i p_i + 2M_{\text{H}_2}} \quad (6)$$

where n_i is the stoichiometry for product i ; p_i is the molar quantity of the product; M_{H_2} is the molar quantity of generated H_2 .

3. Results and discussion

3.1. Characterization

The SEM images showed that BC could be clearly seen and significantly inhibited agglomeration of S-nZVI particles (Fig. S1a-b). The spherical nZVI particles ($<80 \text{ nm}$) that appeared in the TEM as chain-like aggregates still existed in nZVI/BC (Fig. S1c). However, after sulfidation, no obvious aggregation or chain-like particles were observed from TEM due to the formed FeS_x layer (Fig. S1d-f) [44]. Therefore, the sulfidation and BC modification both contributed to dispersion of the nZVI particles. Larger primary particles were observed with an increasing degree of sulfidation compared to nZVI/BC ($<80 \text{ nm}$) (Fig. S1c-f), which was due to the suppression of Fe^0 nucleation and a bloom of Fe^0 crystal growth resulting from $\text{Na}_2\text{S}_2\text{O}_4$ addition [45,46]. Notably, BC seemed to be invisible in S-nZVI/BC (0.035), possibly due to the overlap of BC and flake-like shell structures or the inhomogeneity of particles during characterization (Fig. S1d). A similar phenomenon was reported in previous studies [31,47]. Although there were larger primary particles on S-nZVI/BC surface, its surface area was generally higher than that of nZVI/BC due to increasing surface roughness and the formation of a flake-like structure (Fig. S2) [15]. According to the S and Fe maps, line scans and EDX spectra of S-nZVI/BC (0.090) (Figs. 1a-f and S3), S was distributed throughout the particle (both core and shell area) rather than being enriched on the shell (surface coating) [48]. Iron sulfides were likely formed along with Fe^0 nucleation during S-nZVI_{co} synthesis [46]. In addition, the differences in the S distribution between the core and edge of the particle in different areas were observed based on line scans (Fig. S4), which showed that the core had a lower S/Fe ratio and the edge had a higher S/Fe ratio. Meanwhile, the EDX analysis showed that the S/Fe molar ratio was 0.050 in the core area and 0.057 in the flake-like shell area (Fig. S3b-c), which was consistent with line scans result.

To further clarify the S distribution in bulk particles, systematic XPS depth profiles (i.e., 10, 30, and 60 nm) were performed to determine the general distribution of Fe and S species of S-nZVI/BC (0.090) (Fig. S5a-b). The increasing trend of the S/Fe atomic ratio with increasing analytical depth (i.e., from shell to core) by the XPS analysis showed a reverse trend from the line scan and EDX results (Fig. S5c), presumably because the formed iron oxides on the shell overlapped the S during particle characterization [24]. Importantly, relatively more oxidized forms of Fe (Fe^{3+}) and S species (SO_4^{2-}) were detected on the shell of particles compared to the core of the particles (Fig. 1g-h). Moreover, the fraction of Fe^{3+} dropped from 51.85% to 31.87% as the depth increased from 0 to 60 nm, whereas SO_4^{2-} became undetectable at depths of $\geq 10 \text{ nm}$. Therefore, no oxidized S species were observed ($\geq 30 \text{ nm}$), along with the gradual increase in the signal of reduced Fe species (Fe^{2+} and Fe^0) closer to the core area. In addition, although S_n^{2-} was the dominant species on the shell, S_2^{2-} species became dominant as the depth increased (Fig. 1h). The ICP-OES analysis showed that the actual S/Fe ratio of particles ($[S/Fe]_{\text{particles}}$) increased linearly with the amount of S added during the synthesis ($[S/Fe]_{\text{dose}}$) (Fig. 1i). Nevertheless, the

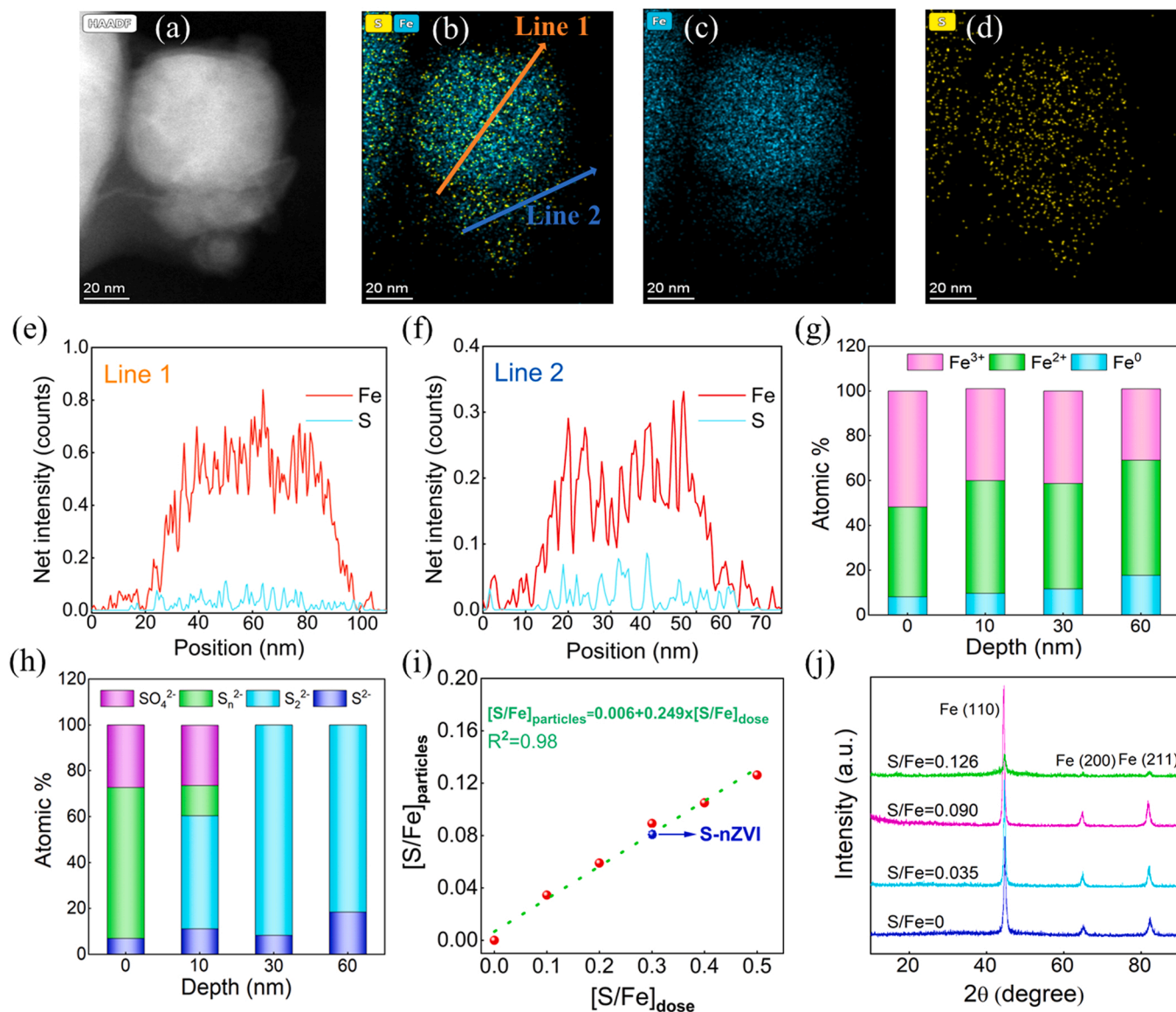


Fig. 1. (a) High-angle annular dark-field (HAADF) images, (b) Fe and S, (c) Fe, (d) S maps, and (e-f) line scan of S-nZVI/BC (0.090) determined by TEM energy-dispersive X-ray (EDX)-mapping analysis. (g) Fe speciation and (h) S speciation distribution of S-nZVI/BC (0.090) in different depth based on XPS analysis. (i) Positively linear correlation of actual $[S/Fe]_{\text{particles}}$ with $[S/Fe]_{\text{dose}}$. (j) XRD spectra of S-nZVI/BC with different $[S/Fe]_{\text{particles}}$.

$[S/Fe]_{\text{particles}}$ were always much lower than the $[S/Fe]_{\text{dose}}$ due to the outgassing of H₂S during synthesis [31]. Thus, it was more important to report and calculate the actual $[S/Fe]_{\text{particles}}$ rather than the $[S/Fe]_{\text{dose}}$, which had been identified as a dominant factor to determine contaminant transformation [5]. Note that the actual S/Fe ratio of S-nZVI/BC (0.090) was higher than that of S-nZVI (0.082) at the same $[S/Fe]_{\text{dose}}$ (0.3), suggesting that BC might improve the sulfidation efficiency (Fig. 1i), possibly because BC promoted the dispersion of S-nZVI particles (Fig. S1b,e) and hence increased the degree of sulfidation.

The effect of the amount of incorporated S on the crystalline properties of nZVI/BC was investigated by XRD, including the lattice constant, crystalline domain size (D), and lattice spacing (d) (Figs. 1j and S6). Specifically, three Fe peaks ((110), (200), and (211)) observed for S-nZVI/BC (0.035 and 0.090) had higher intensity and were shifted leftwards compared to nZVI/BC, especially for S-nZVI/BC (0.090) (Fig. S6a-c). In addition, the crystalline domain sizes larger than nZVI/BC were also observed for all Fe planes in the Fe⁰ body-centered-cubic (BCC) structure for $[S/Fe]_{\text{particles}} = 0.035$ and 0.090 (Fig. S6d-f). However, further increasing $[S/Fe]_{\text{particles}}$ to 0.126 resulted in a decrease in peak

intensity and crystalline scattering domain size, indicating that excessive S likely disturbed the Fe⁰ BCC structure [25]. Moreover, the d-spacing of all Fe planes of S-nZVI/BC were larger than nZVI/BC (Fig. S6g-i). Notably, the peak intensity and D value of S-nZVI/BC were higher than those of nZVI/BC, except for S-nZVI/BC (0.126), indicating that sulfidation (S-nZVI_{co}) significantly improved the crystallinity [5]. The above results (i.e., the change of lattice constant, crystalline domain size, peak position, and lattice spacing) suggested that the incorporation of S into the Fe⁰ BCC structure by S-nZVI_{co} method formed a solid solution (alloy compound), which was consistent with previous studies [15,25,49,50]. Typically, a smaller lattice constant corresponds to a smaller interatomic distance, which is inversely proportional to the band gap and requires more energy to release the valence electrons [23]. The presence of iron sulfides with a lower band gap than iron oxides and distorted lattice constant would significantly affect the electron-transfer resistance, as discussed below [43].

3.2. Performance of S-nZVI/BC in TBBPA transformation and its pathway

As shown in Fig. 2a, almost all TBBPA was degraded within 24 h by S-nZVI/BC and S-nZVI except for nZVI/BC, along with the formation of four debromination products (i.e., tri-BBPA, di-BBPA, mono-BBPA, and BPA) (Fig. 2b-e). Conspicuously, there was a significant advantage of S-nZVI/BC (0.090) over S-nZVI/BC (0, 0.035, and 0.126) and S-nZVI (0.082) concerning their degradation rate of TBBPA. Sulfidation coupled with BC greatly enhanced the performance of nZVI for reductive degradation of TBBPA. The specific reinforcement mechanism was discussed later. Overall, the fraction of TBBPA continuously decreased, and the fraction of tri-BBPA, di-BBPA, and mono-BBPA showed a similar trend that first increased to peak values and then gradually dropped as reaction proceeded (Fig. 2b-d). Meanwhile, the fraction of BPA increased steadily as reaction proceeded (Fig. 2e). For instance, for S-nZVI/BC (0.090), TBBPA was completely degraded, and the fraction of BPA continuously increased to approximately 40% after 24 h, while tri-BBPA, di-BBPA, and mono-BBPA increased initially, reached a maximum at 4, 9, and 12 h, and then decreased as time proceeded (Fig. 2f). Briefly, this result revealed that the debromination of TBBPA by S-nZVI/BC and S-nZVI was a consecutive reaction and that the introduction of BC did not alter the degradation pathway [51,52]. As a result, the transformation pathway of TBBPA was proposed (Fig. S7). The lower-than-expected mass balance was probably due to irreversible sorption of contaminants to BC despite three methanol extractions (Fig. 2f) [31].

3.3. Factors affecting TBBPA reactivity by S-nZVI/BC

Important factors influencing the reactivity of S-nZVI/BC for TBBPA degradation were investigated, including $[S/Fe]_{\text{particles}}$ molar ratio, S-

nZVI/BC dosage, initial TBBPA concentration, and initial pH (Figs. 3 and S8a-c). The kinetic curves of TBBPA degradation by S-nZVI/BC were well fitted with the pseudo-first-order reaction rate model, in accord with previous studies [38,53]. The reactivity of S-nZVI/BC for TBBPA degradation was assessed by the surface-area-normalized rate constant ($k_{SA, TBBPA}$) (Table S4). The $[S/Fe]_{\text{particles}}$ molar ratio of S-nZVI/BC was a crucial factor in determining its physicochemical properties (e.g., lattice constant, charge-transfer resistance, and S speciation/content), which was correlated with the reactivity and selectivity of S-nZVI/BC in TBBPA transformation (Fig. 3a), as discussed below. As shown in Fig. 3b and Table S4, a higher dosage of particles provided more reactive sites for TBBPA and thus had a higher $k_{SA, TBBPA}$. Fig. 3c and Table S4 showed that the $k_{SA, TBBPA}$ decreased remarkably from 6.52×10^{-3} to $1.96 \times 10^{-3} \text{ L m}^{-2} \text{ h}^{-1}$ as the initial TBBPA concentration increased from 5 to 20 mg L^{-1} , suggesting that there were excess TBBPA molecules for available reactive sites [38]. Furthermore, the abundant TBBPA or its degradation products might also deactivate the surface-active sites in surface-mediated reactions [54]. Notably, the reaction between S-nZVI and contaminants was a rapid process. The S-nZVI dispersed by BC reacted quickly with TBBPA when the S-nZVI/BC was excessive. However, when TBBPA was abundant enough, the reaction entered the slow transfer stage after the surface S-nZVI was consumed. At this time, the reaction rate depended on the slow contact reaction between the TBBPA and the active components inside the S-nZVI. Therefore, the degradation rate decreased (Fig. 3c). However, the overall degradation efficiency of S-nZVI/BC was still up to 88% and higher than that of S-nZVI (73%) when the concentration of TBBPA was 20 mg L^{-1} (Fig. S8d), confirming that the support of BC was conducive to the reaction between TBBPA and the surface-active components and more conducive to the reaction with the internal-active components of S-nZVI. Overall, at high concentrations of TBBPA, the reaction rate was delayed, but the reaction capacity might be improved (slow release). The pH was supposed to significantly affect the

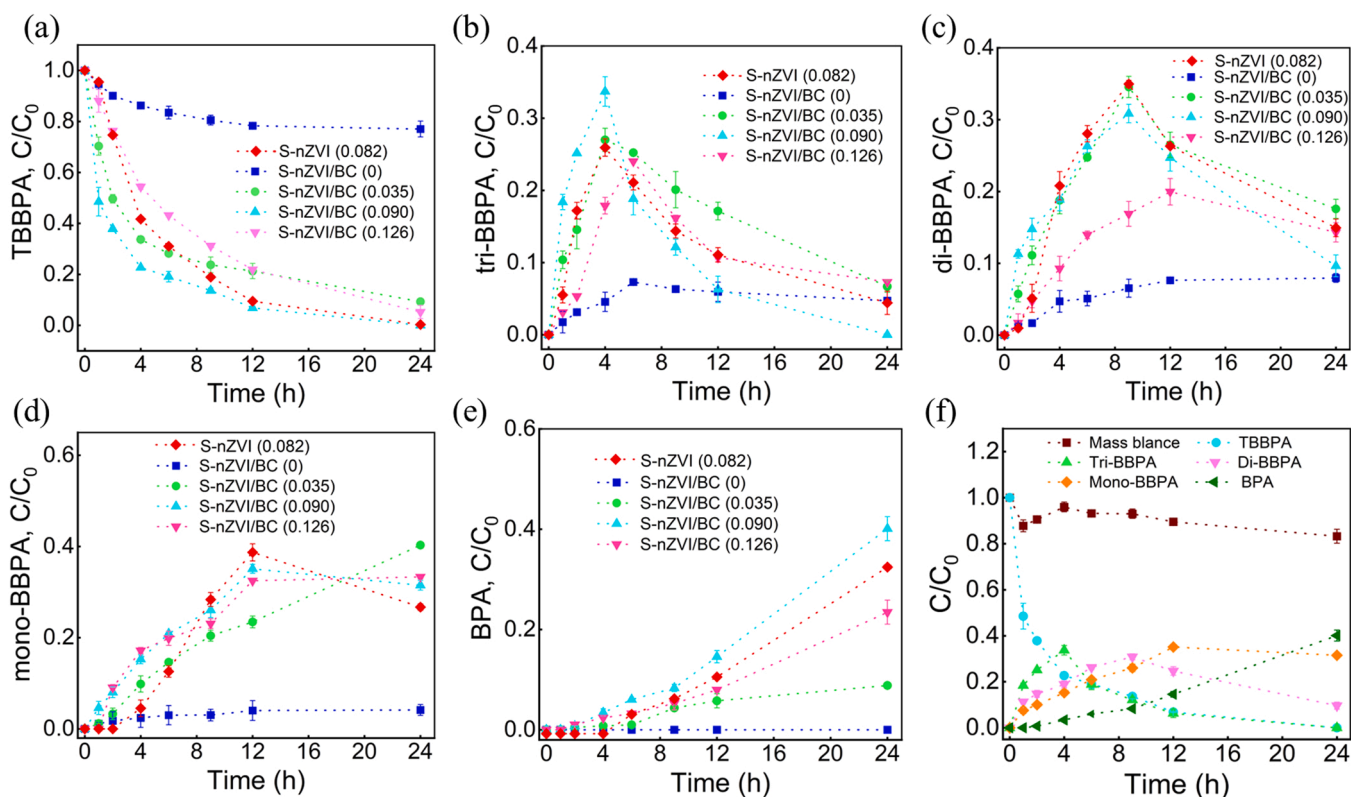


Fig. 2. Degradation kinetics of (a) TBBPA and generation kinetics of (b) tri-BBPA, (c) di-BBPA, (d) mono-BBPA, and (e) BPA of TBBPA degradation by S-nZVI/BC with different $[S/Fe]_{\text{particles}}$ and S-nZVI. (f) Mass balance of TBBPA and degradation products for S-nZVI/BC (0.090). Basic conditions: reaction time = 24 h, initial pH = 7.0, $T = 25^\circ \text{C}$, 10 mg L^{-1} TBBPA, and 2.0 g L^{-1} S-nZVI/BC (0.090) or 1.5 g L^{-1} S-nZVI (0.082).

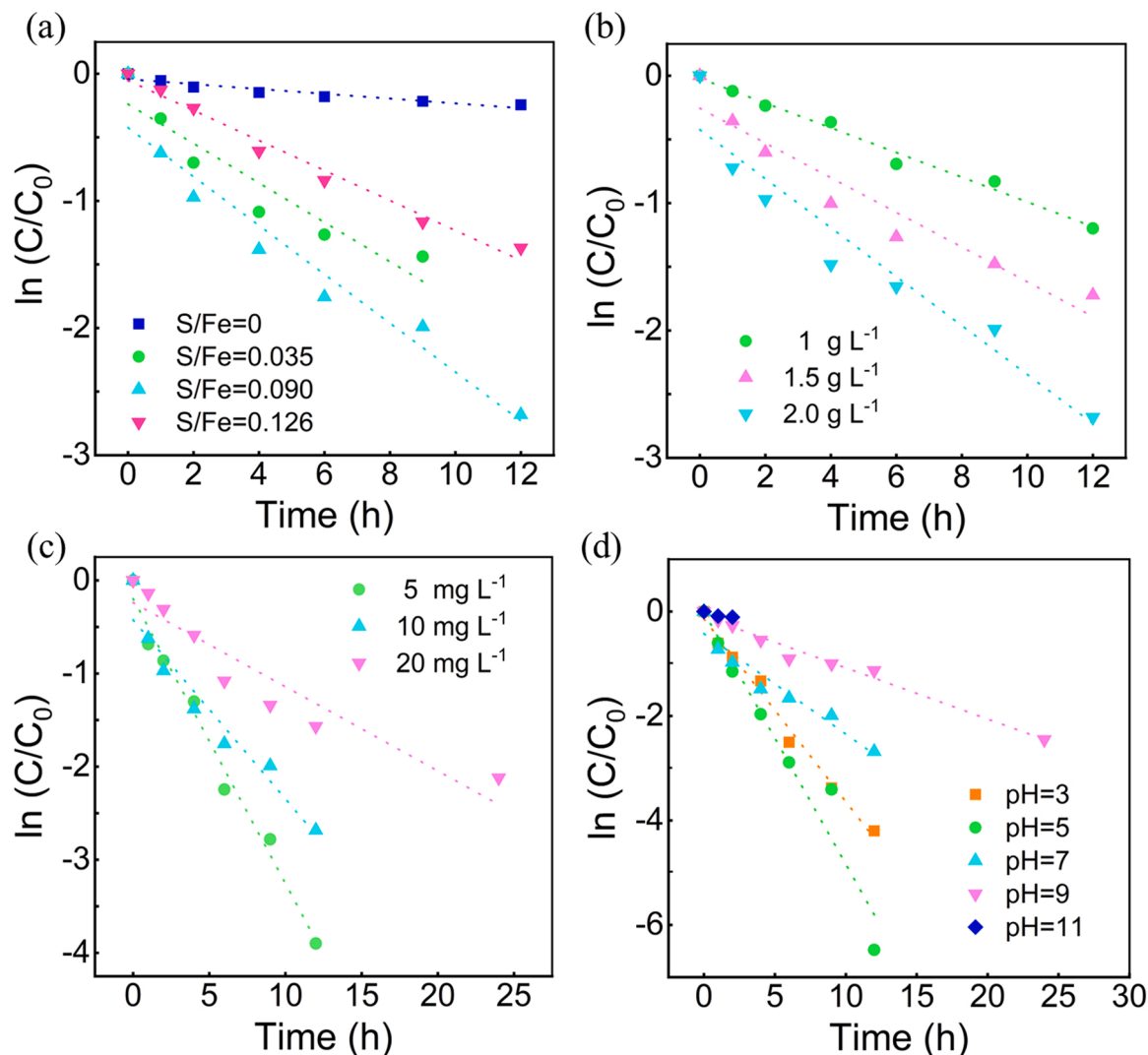


Fig. 3. Effects of (a) $[S/Fe]_{\text{particles}}$ molar ratio (b) S-nZVI/BC dosage, (c) initial TBBPA concentration, and (d) initial pH on the TBBPA degradation rate. Basic conditions: reaction time = 24 h, initial pH = 7.0, $T = 25^\circ\text{C}$, 10 mg L^{-1} TBBPA, and 2.0 g L^{-1} S-nZVI/BC (0.090).

surface properties of particles (e.g., corrosion and passivation) to control interfacial reactions [55]. On the whole, the $k_{SA,TBBPA}$ decreased with increasing pH from 5 to 11. Besides, TBBPA was completely degraded under neutral or acidic pH conditions (i.e., pH = 7 and 5) (Fig. S8c), and the $k_{SA,TBBPA}$ increased from 4.27×10^{-3} to $1.04 \times 10^{-2}\text{ L m}^{-2}\text{ h}^{-1}$ as the pH decreased from 7 to 5 (Fig. 3d and Table S4) and then marginally decreased as the pH lowered to 3 ($7.57 \times 10^{-3}\text{ L m}^{-2}\text{ h}^{-1}$). Therefore, a typical acid-driven process was obtained in which a low pH (i.e., pH = 5) accelerated dissolution of the surface passivation layer by adequate H^+ and hence exposed more active sites for TBBPA transformation [56]. At extremely acidic environment (i.e., pH = 3), the decrease in $k_{SA,TBBPA}$ occurred because electrons (e^-) were rapidly consumed by H^+ to form H_2 rather than transformed to TBBPA. Meanwhile, the concentration of H_2 was up to $9.05 \times 10^{-1}\text{ mmol}$ (Table S5), which further confirmed that a large amount of H_2 formed on the particle surface that may act as a barrier preventing the TBBPA from contacting the S-nZVI/BC surface [39,57]. Notably, the degradation efficiency was 91.4% at pH = 9 and only 16% with a $k_{SA,TBBPA}$ of $1.16 \times 10^{-3}\text{ L m}^{-2}\text{ h}^{-1}$ at pH = 11 (Fig. S8c and Table S4), which was because the formed iron (oxy)hydroxide precipitates on the S-nZVI/BC surface occupied the reaction sites under alkaline conditions [37,57].

3.4. Core reactivity upon sulfidation

Both $[S/Fe]_{\text{particles}}$ and $[S/Fe]_{\text{surface}}$ are likely to be crucial for enhanced reactivity, with the former determining the electron transfer from the Fe core to surface and the latter controlling surface reaction [26]. Specially, the $[S/Fe]_{\text{particles}}$ and $[S/Fe]_{\text{surface}}$ represented the S/Fe atomic ratio in the bulk and on the surface (shell), respectively. According to XPS analysis (Fig. S9), the $[S/Fe]_{\text{surface}}$ increased with increasing $[S/Fe]_{\text{particles}}$ (Fig. S9c). At lower values of $[S/Fe]_{\text{particles}}$ (≤ 0.090), S_n^{2-} and SO_4^{2-} were the dominant species on the shell of particles, while S^{2-} showed a sharp increase with formation of S_2^{2-} up to 14.62 atom% as $[S/Fe]_{\text{particles}}$ increased from 0.090 to 0.126 (Fig. 4a). It was noteworthy that the oxidative S species (SO_4^{2-}) did not favor the reactivity [58]. Interestingly, at $[S/Fe]_{\text{particles}} = 0.090$, S^{2-} was only 6.97 atom% and S_n^{2-} was as high as 65.71 atom%, presumably because of the conversion of S^{2-} to S_n^{2-} [29]. The majority of S on the shell of S-nZVI/BC (0.126) was in the reduced forms (e.g., S^{2-} , S_2^{2-} , and S_n^{2-}) (Fig. 4a), which were expected to enhance reactivity [25,59,60]. Generally, the reduced S species of the shell are hydrophobic and have a low band gap, which have stronger affinity toward hydrophobic groups and facilitate electron transfer from Fe^0 to the contaminants [24]. However, the increasing trend of S content (Fig. S9c) and reduced S species (Fig. 4a) in the shell of particles did not correlate well with the reactivity of S-nZVI/BC for

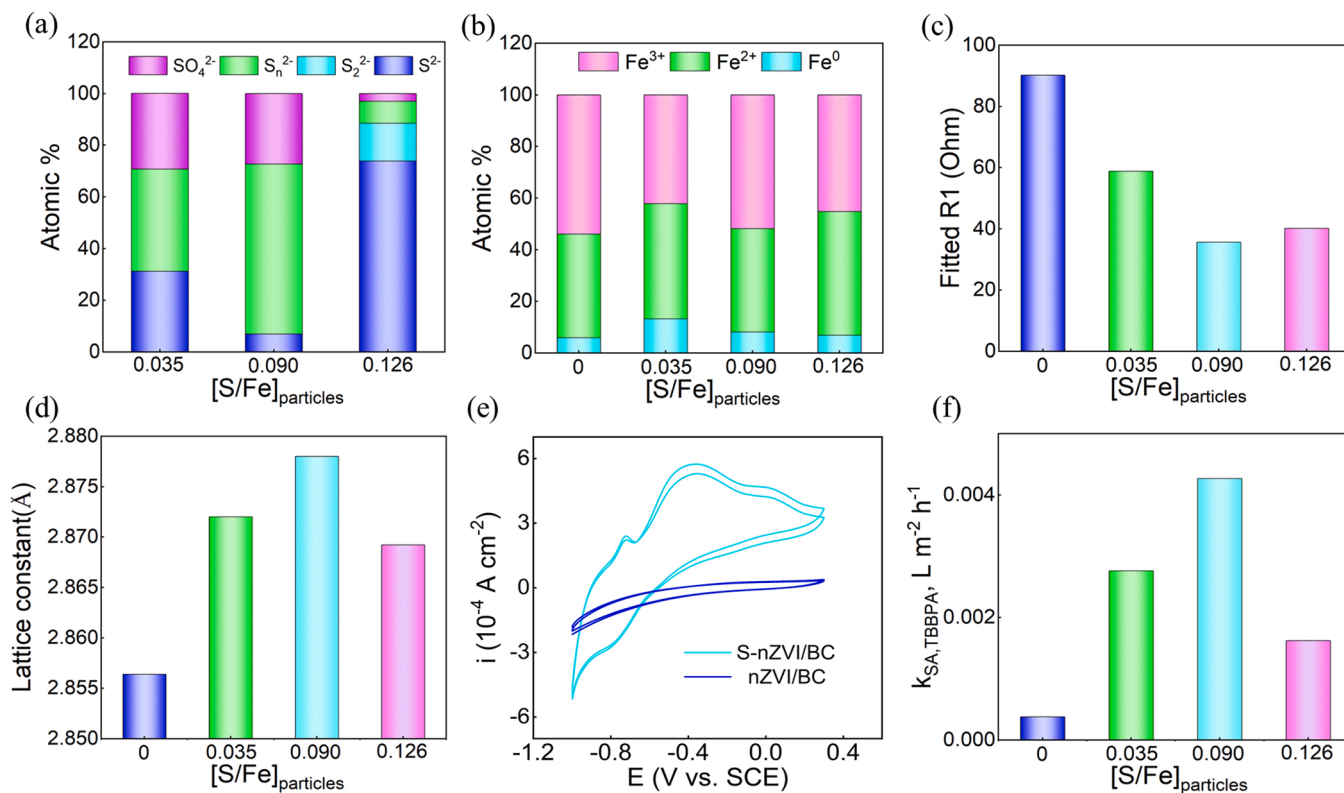


Fig. 4. (a) Surface S speciation distribution and (b) surface Fe speciation distribution of S-nZVI/BC with different [S/Fe]_{particles} based on XPS analysis, (c) fitted resistance R1 and (d) lattice constants of S-nZVI/BC with different [S/Fe]_{particles}. (e) CV cycle profiles with S-nZVI/BC (0.090 and 0). (f) *k*_{SA,TBBPA} of S-nZVI/BC with different [S/Fe]_{particles}.

TBBPA degradation with the increase of [S/Fe]_{particles}, suggesting that the shell properties of particles were not an important factor in reactivity, as discussed below. For sulfidated nZVI/BC, Fe species (e.g., Fe⁰, Fe²⁺, and Fe³⁺) in the shell were generally similar for various [S/Fe]_{particles}. In contrast, nZVI/BC possessed the lowest Fe⁰ (5.87%) and highest Fe³⁺ content (53.89%) (Fig. 4b), indicating improved antioxidation property after sulfidation.

Sulfidation has been hypothesized to facilitate electron transfer in previous studies, but the specific causes were rarely reported [38,61]. The charge-transfer resistance (R1) of S-nZVI/BC with different [S/Fe]_{particles} was probed by electrochemical impedance spectroscopy (EIS). Nyquist plots were fitted to an equivalent circuit model to derive resistance R1, including the electron-transfer resistance and contact resistance. (Fig. S10) [25]. Since all materials were prepared under the same conditions during characterization, the contact resistance was considered to be similar, and R1 well reflected their differences in electron-transfer resistance. The R1 of all S-nZVI/BC was lower than that of nZVI/BC with the lowest R1 for S-nZVI/BC (0.090) (Fig. 4c), suggesting that sulfidation markedly decreased the electron-transfer resistance. Analysis of the band gaps for iron sulfides (e.g., FeS=0.10 eV, FeS₂=0.95 eV, and Fe₃S₄=0.00 eV) and iron oxides (e.g., FeO=2.40 eV, Fe₂O₃=2.20 eV, Fe₃O₄=0.10 eV, and FeOOH=2.60 eV) indicated faster electron transfer of iron sulfides than iron oxides [5]. However, compared to S-nZVI/BC (0.090), S-nZVI/BC (0.126) possessed a higher R1 despite a higher S content (Fig. S9c) and more proportion of reduced S species (i.e., S²⁻, S₂²⁻, and S_n²⁻) on the shell (Fig. 4a). In addition, the higher R1 of S-nZVI/BC (0.126) was also associated with a lower conductive metal Fe⁰ content (mainly in the core) (Fig. S11) [43]. Notably, controlling S content might alter distribution of S species (e.g., S²⁻, S₂²⁻, and S_n²⁻) in core in addition to that on shell [25], and the former might be more influential than the latter on R1. Thus, the core properties (e.g., S speciation/content and Fe⁰ content) instead of shell properties seemed to be a determining factor for R1, which was closely related to

the e-mediated mechanism for TBBPA debromination, as discussed below. It is noteworthy that S incorporation extended the Fe⁰ BCC lattice constant and thus lowered the electron-transfer resistance [25,62,63]. The S-nZVI/BC (0.090) had a maximum lattice constant, which facilitated electron transfer (Fig. 4d). Furthermore, the redox peak also had a higher current density than that of nZVI/BC (Fig. 4e), further confirming the higher electron transfer efficiency of S-nZVI/BC (0.090) than nZVI/BC [64]. These results indicated that the electron transfer of S-nZVI/BC depended on the specific physicochemical properties (e.g., lattice constant, Fe⁰ content, and S speciation/content).

Generally, the hydrophobicity of particles appeared to be an important factor for selectivity and reactivity, which made it possible for particles to selectively anchor the contaminants of concern and minimize the HER, especially for hydrophobic groups on contaminants (e.g., halogen groups) [28,38]. As shown in Figs. S12a-f and S13, the water contact angles of S-nZVI/BC with different [S/Fe]_{particles} (0, 0.035, 0.059, 0.090, 0.105, and 0.126) were 27 ± 0.3°, 44 ± 0.3°, 52 ± 0.5°, 54 ± 0°, 42 ± 0.3°, and 35 ± 0.5°, respectively, which was first increased and then decreased as the increase of [S/Fe]_{particles} molar ratio and thus the water contact angle of particles might depend on the content of S incorporated into the structure [25]. Note that neither the lowest nor the highest [S/Fe]_{particles} material showed the highest hydrophobicity, which was consistent with previous studies [25]. On the whole, compared to unsulfidated nZVI/BC, sulfidated nZVI/BC had a higher hydrophobicity, which contributed to the improvement of reactivity and selectivity, as discussed below. Herein, the difference of the water contact angles in different sulfidated nZVI/BC was determined by various possible factors (e.g., the S/Fe speciation, the crystalline structure, and the coordination between S and Fe) in addition to S content [24,65]. For example, pyrite (FeS₂) was more hydrophobic than mackinawite (FeS) in the particles [55]. Impressively, in addition to the hydrophobicity, blocking of H adsorption sites and decreasing electron transfer both contribute to suppressing the HER [25].

The reactivity of S-nZVI/BC with different amount of incorporated S with TBBPA was determined to explore the degradation mechanism. As shown in Fig. 4f, the $k_{SA,TBBPA}$ of S-nZVI/BC with different [S/Fe]_{particles} molar ratio (0, 0.035, 0.090, and 0.126) was 3.77×10^{-4} , 2.76×10^{-3} , 4.27×10^{-3} , and $1.62 \times 10^{-3} \text{ L m}^{-2} \text{ h}^{-1}$, respectively. Regardless, there was a remarkable advantage of the sulfidated nZVI/BC over the unsulfidated nZVI/BC with respect to the reactivity with TBBPA, which resulted from its higher hydrophobic and lower charge-transfer resistance. Besides, the reactivity of S-nZVI/BC (0.090) was the highest, which was ≈ 11.3 and ≈ 1.5 – 2.6 times higher than that of nZVI/BC and other S-nZVI/BC, respectively. The highest reactivity for S-nZVI/BC (0.090) was predominantly attributed to lower charge-transfer resistance (Fig. 4c) and higher expanded lattice (Fig. 4d) (both facilitated electron transfer). Notably, although there was higher water contact angle of S-nZVI/BC than nZVI/BC, the particles were still hydrophilic (Fig. S13), indicating that hydrophobicity might be not a major factor in reactivity, while significantly improved electron transfer efficiency upon sulfidation played a dominant role in reactivity. Importantly, although the reduction of contaminants by S-nZVI/BC was generally considered a surface reaction, the core properties determined the overall electron transfer efficiency from Fe core to the reactive surface. This further illustrated the importance of direct electron transfer (e-mediated) in TBBPA degradation. The lowest reactivity of S-nZVI/BC (0.126) was likely because the thicker passivating layer formed at higher [S/Fe]_{particles} blocked the surface reactive sites and reduced electron transfer efficiency [61]. Impressively, although S-nZVI/BC (0.126) had more S content (Fig. S9c) and more reduced sulfur species on the shell than S-nZVI/BC (0.090) (Fig. 4a), the lower reactivity revealed the lack of a clear relationship between shell properties (e.g., S speciation/content) and the reactivity. The $k_{SA,TBBPA}$ reached the maximum at [S/Fe]_{particles} = 0.090, inconsistent with reported studies of optimal S/Fe ratios (e.g., 0.025 for TCE and 0.51 for TBBPA), possibly because of addition of BC or differences in contaminants [18,38]. The actual degradation rate might depend on a combination of various factors (e.g., electron transfer, hydrophobicity, S content) for the specific modification materials (e.g., S-nZVI/BC) synthesized in different studies. Any changes in these factors would affect the degradation rate of the investigated contaminants.

To enhance the understanding of the degradation mechanism, XPS and XRD were carried out for particles before and after the reaction (Figs. S14–S16). Note that XPS without ion sputtering (depth profiling) only detected shell speciation, and XRD revealed bulk properties [61]. For S-nZVI/BC, no obvious differences in S species on the shell were observed after the anoxic reaction (Fig. S14a,c), suggesting that the S species only acted as an electron conductor and did not serve as the electron donor for TBBPA debromination. However, the S species on the shell in S-nZVI system might act as a reducing agent toward different contaminants (e.g., NB, Cr (VI), Se (VI), and HBCD) [17,31,66,67]. The fraction of Fe⁰ and Fe³⁺ species of the shell decreased from 8.12% and 51.85% to 6.06% and 47.24% respectively and Fe²⁺ species increased from 40.04% to 46.70% before and after reaction (Fig. S14b,d). However, for S-nZVI, S²⁻ showed a sharp decrease with formation of S_n²⁻ after reaction due to the oxidation of the shell (i.e., S²⁻ was oxidized into S_n²⁻) (Fig. S15a,c) [14]. In addition, the fraction of Fe⁰ and Fe²⁺ species of the shell slightly decreased, while Fe³⁺ species increased after reaction (Fig. S15b,d). In brief, before and after the reaction, S-nZVI/BC always had more Fe⁰ and less SO₄²⁻ than S-nZVI, illustrating that the presence of BC could retard the oxidation of S-nZVI (Figs. S14 and S15) [31]. XRD analysis showed that there was a slight decrease in the peak intensity for Fe⁰ of S-nZVI/BC after 24 h reaction with TBBPA (Fig. S16), indicating that the particle still maintained its reactivity. However, some weak peaks for iron oxide (FeO and Fe₂O₃) appeared after reaction, suggesting that only a small portion of Fe⁰ reacted with TBBPA, and the reaction of Fe⁰ with H₂O was slowed by S modification [54].

3.5. Enhanced selectivity upon sulfidation

As shown in Fig. 5a, the electron efficiency (i.e., selectivity) of nZVI/BC for TBBPA degradation was significantly enhanced after sulfidation likely due to its higher hydrophilicity (Fig. S13) and blocking of H adsorption sites, which was ~ 78.9 – 152.6 times higher than that of unsulfidated nZVI/BC (0.038%). For sulfidated nZVI/BC, although the hydrophobicity of S-nZVI/BC (0.090) was the highest in different [S/Fe]_{particles} (Fig. S13), the selectivity of S-nZVI/BC (0.090) (4.7%) for TBBPA degradation was lower than that of S-nZVI/BC (0.126) (5.8%). This was because S content of S-nZVI/BC (0.090) was lower than that of S-nZVI/BC (0.126) (Fig. 1i), which resulted in more H adsorption sites. However, the selectivity of S-nZVI/BC (0.126) was the highest, even though it was more hydrophilic (Fig. S13) and had poor reactivity with TBBPA (Fig. 4f). This was likely because the increased S content blocked more H adsorption sites and thus markedly inhibited the HER, which was extensively quantified through density functional theory (DFT) calculations [2,20,43]. The more significant decrease in the reaction rate with water led to superior selectivity compared to the decrease in the reaction rate of TBBPA. In addition, the water contact angle of S-nZVI/BC (0.035) was slightly larger than that of S-nZVI/BC (0.126), but it remained hydrophilic (Fig. S13). Therefore, the lowest selectivity of S-nZVI/BC (0.035) (3.0%) upon sulfidation might be attributed to the lowest [S/Fe]_{particles} (Fig. 1i) in addition to higher hydrophilicity, resulting in more H adsorption sites than those with higher S content. Generally, the electron efficiency positively correlates with hydrophobicity [25,43]. However, the results of this study indicated that [S/Fe]_{particles} could be used as an indicator of electron efficiency when the particles were more hydrophilic (Fig. S17), further advancing the understanding of selectivity. Thus, for more hydrophilic S-nZVI/BC, the hydrophobicity of particles was not a determining factor for selectivity. Rather, the optimum electron efficiency endowed by sulfidation might occur, at where the properties (e.g., hydrophobicity, electron transfer, and blocking H adsorption sites) might work in synergy that made the S-nZVI/BC less reactive with water, but increased the reactivity with TBBPA. Additionally, the electron efficiency could be affected by the material/contaminant ratio, e.g., the decrease in contaminant concentration brought about a decreasing fraction of electrons from Fe⁰ to contaminant relative to the stable reaction with water [26,43,68]. Therefore, the highest electron efficiency (5.8%) in this study was higher than that in previous literature (1.1%) for TBBPA degradation, which might be due to the lower S-nZVI/BC/TBBPA ratio [53].

The dominant mechanism (H-mediated versus e-mediated) in dehalogenation of HOCs in the sulfidation system has long been debated [2]. Herein, the relative importance of atomic H and direct electron transfer was explored by quenching experiments using TBA and comparison experiment with D₂O instead of H₂O as reaction medium. As shown in Fig. 5b, the degradation became slightly slower after the addition of TBA, and there was no significant difference among the fitting linear at different concentrations of TBA (1–200 mM). Besides, it could be found that TBBPA degradation was also inhibited slightly after replacing H₂O with D₂O as reaction medium (Fig. S18). The above results suggested that a minority of debromination was attributed to atomic H while most occurred via direct electron transfer. Accordingly, it was concluded that the e-mediated mechanism dominated TBBPA debromination in the sulfidation system, and sulfidation probably more favored e-mediated reduction. On the contrary, the greater improvement in reactivity was attributed to the effect of atomic H (H-mediated) in the bimetallic system [39,69,70]. The discrepancy in mechanism between the two systems might occur because the presence of S hindered H adsorption and attracted electronic charge from nearby Fe sites, which supported e-mediated reduction [2].

In summary, the proposed debromination mechanisms did not act alone; instead, the atomic H and direct electron transfer might mediate the reaction simultaneously and distinct dominant roles might be applicable to different contaminants. Most of the electrons provided by

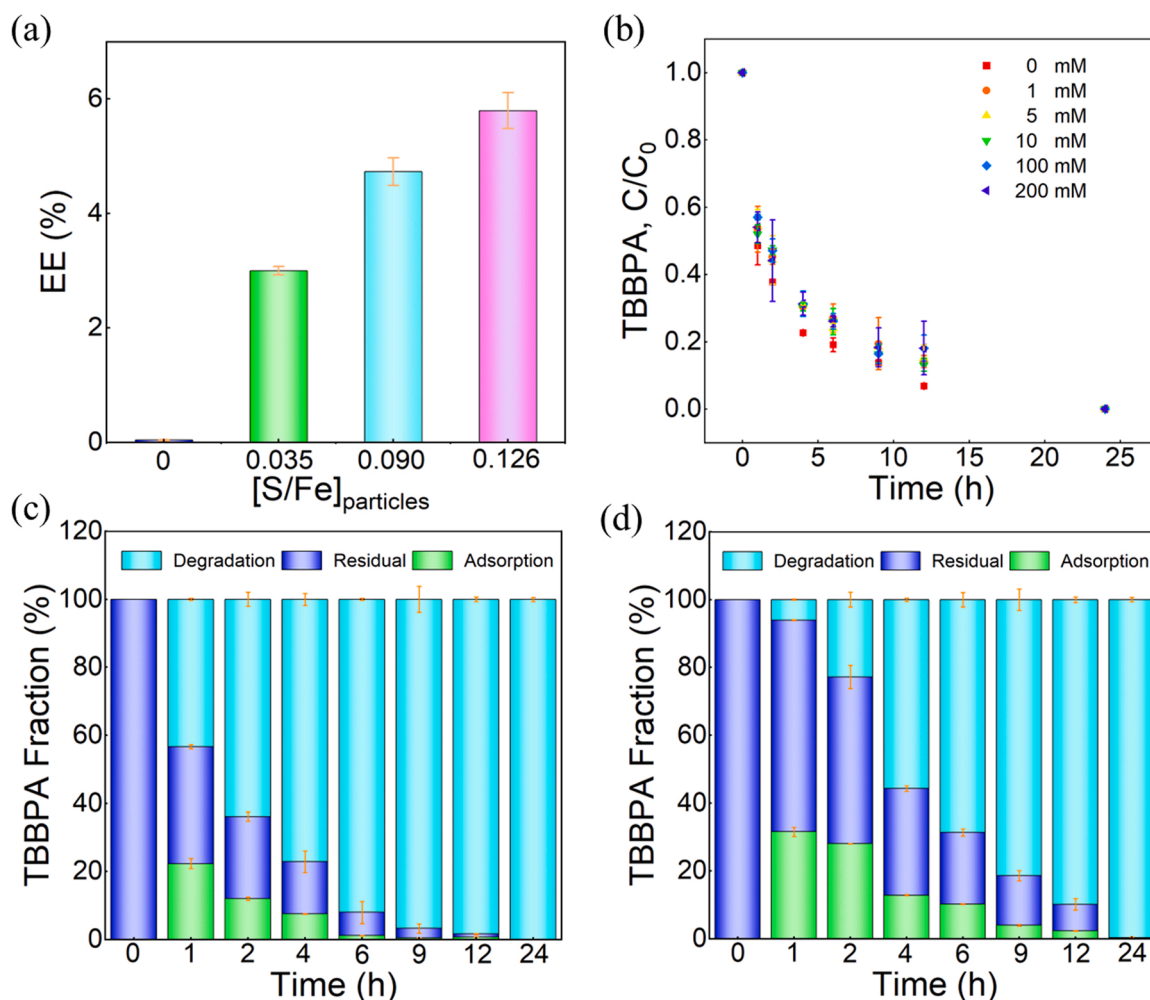


Fig. 5. (a) Electron efficiency (EE) of S-nZVI/BC with different $[S/Fe]_{\text{particles}}$. (b) Kinetics of TBBPA degradation in the presence of TBA. The fraction of TBBPA debromination, residual, and adsorption in (c) S-nZVI/BC and (d) S-nZVI reaction systems. Basic conditions: reaction time = 24 h, initial pH = 7.0, $T = 25^\circ\text{C}$, 10 mg L^{-1} TBBPA, and 2.0 g L^{-1} S-nZVI/BC (0.090) or 1.5 g L^{-1} S-nZVI (0.082).

Fe^0 for TBBPA debromination were transferred to TBBPA by direct electron transfer, and a few were first transferred to hydrogen protons (Volmer reaction) and then mediating debromination.

3.6. Role of the BC and TBBPA distribution in different phases

The reactivity of S-nZVI/BC for TBBPA degradation was higher than that of S-nZVI through BC modification at the same $[S/Fe]_{\text{dose}}$ (0.3) (Fig. S19). As shown in Fig. S20a-b, the decreased oxidative S species (SO_4^{2-}) and increased reduced Fe species (Fe^{2+} and Fe^0) in S-nZVI/BC compared to S-nZVI indicated that the presence of BC could retard the oxidation of S-nZVI. In addition, S-nZVI/BC had better electron transfer efficiency than S-nZVI due to the higher current density (Fig. S20c) and smaller semicircle diameter (Fig. S20d), which could be attributed to BC modification. The measured water contact angles were approximately $54 \pm 0^\circ$ and $33 \pm 0.9^\circ$ for S-nZVI/BC and S-nZVI (Fig. S20e), respectively. Therefore, BC carrier improved the hydrophobicity of S-nZVI. Additionally, surface functional groups (e.g., carbonyl groups) and condensed polyaromatic carbon matrices in BC were major components that were responsible for the enhanced electron transfer [35]. Thus, BC might serve as electron shuttle, and the conductive ability determined the rates of galvanic corrosion of iron and reduction of adsorbed TBBPA and production of H_2 . Notably, S-nZVI/BC had a higher electron efficiency (4.7%) than S-nZVI (2.0%) (Fig. S20f), probably because BC increased TBBPA reduction to a greater extent than H_2 formation

according to the definition of EE [71]. In summary, it was reasonable to observe that the addition of BC with conductive properties more favorably enhanced reactivity and selectivity of S-nZVI toward TBBPA.

The distribution of TBBPA in different phases was investigated to assess the enhancing function of BC for degradation. The high specific surface area of the particles caused by the BC carrier helped to concentrate contaminants on surface of S-nZVI/BC, which facilitated the reaction of contaminants with the active sites. Besides, the hydrophobic sites, pore structure, and surface functional groups of BC might be used as active sites to accelerate the adsorption of TBBPA and thus react more quickly with S-nZVI [57]. Moreover, BC could result in higher $[S/Fe]_{\text{particles}}$ ratio. The S sites were hydrophobic and tended to block H adsorption, while the Fe sites were hydrophilic in S-nZVI [65]. Therefore, the S can adsorb more TBBPA and largely enable more electrons to be transferred from Fe^0 to TBBPA. Furthermore, XPS C 1 s spectra and O 1 s spectra were used to illustrate the types of surface functional groups to better understand the surface properties (Fig. S21). The type and content of surface functional groups of S-nZVI/BC did not change significantly before and after reaction. The C 1 s spectra showed three peaks at 284.8, 285.9, and 289.2 eV, which were assigned to aromatic or aliphatic carbon (C-C/C-H), phenolic and alcohol carbon (C-O), and O-C=O, respectively (Fig. S21a) [31]. The O 1 s spectra were deconvoluted into three peaks at 530.1, 531.7 and 533.7 eV, which were assigned to C-O, -OH and C=O, respectively, (Fig. S21b) [72]. TBBPA was adsorbed onto BC through interactions with these functional groups

[57].

As shown in Fig. 5c-d and Tables S6 and S7, although S-nZVI/BC had lower adsorption content of TBBPA than S-nZVI as the reaction proceeded, the degradation efficiency was higher. This was because BC significantly accelerated the diffusion of TBBPA to the active sites of S-nZVI and the mass-transfer process of its degradation products, thus enhancing the degradation efficiency. The TBBPA adsorbed on BC was gradually degraded as the adsorption-degradation process proceeded until the complete degradation of TBBPA. In addition, the transformation of TBBPA was accompanied by the formation of free Br ions. Notably, the measured Br ions concentration (4.13 mg L^{-1}) was lower than the theoretical Br ions concentration (4.44 mg L^{-1}) as the reaction proceeded (Fig. S22), which might be ascribed to the adsorption of Br ions by the formed iron hydroxides [73].

4. Conclusion and environmental implications

A core-shell structure of S-nZVI deposited on BC support (S-nZVI/BC) was designed and synthesized to degrade TBBPA in groundwater. The characterization results indicated that the amount of S incorporated into the Fe^0 BCC crystalline structure. The physicochemical properties of S-nZVI/BC, including the crystalline structure, lattice constant, charge-transfer resistance, and shell S speciation/content, well explained the reactivity and selectivity of S-nZVI/BC with different $[\text{S}/\text{Fe}]_{\text{particles}}$ during reductive debromination of TBBPA. The introduction of BC improved the sulfidation efficiency, electron transfer efficiency, hydrophobicity, and prevented the oxidation of S-nZVI and also enhanced degradation of TBBPA. Both atomic H and direct electron transfer could mediate debromination, with the latter dominating. Instead of shell properties, the core properties (e.g., S speciation/content) played a leading role in reactivity. Furthermore, the $[\text{S}/\text{Fe}]_{\text{particles}}$ could be used as an indicator for electron efficiency when the particles were more hydrophilic. The main role of incorporated S was to greatly decrease electron-transfer resistance and improve lattice constant, which markedly facilitated the electron transfer. This further suggested that TBBPA debromination was mostly attributed to direct electron transfer (e-mediated).

From the perspective of mechanism research, the effects of sulfidation alone and BC carrier alone were stated in this study to better understand their coupled effect on the performance of nZVI in TBBPA degradation, which benefited the investigation of nZVI-based technology in the future. Overall, insights into the mechanism of S-nZVI/BC for the reduction remediation of TBBPA would advance the application of nanomaterials with high reactivity and selectivity in groundwater systems. Nonetheless, the effects of the addition of different sulfidation agents on the structure of BC were unknown, which might affect the overall properties of the material. In addition, the feasibility of actual groundwater treatment by S-nZVI/BC also lacked relevant data. These issues need to be addressed in future studies.

CRediT authorship contribution statement

Feilong Gao: Conceptualization, Methodology, Writing – original draft. **Honghong Lyu:** Methodology, Data curation. **Shakeel Ahmad:** Data curation. **Siyu Xu:** Data curation. **Jingchun Tang:** Writing – review & editing, Supervision, Resources.

Declaration of Competing Interest

The authors declare that they have no known competing financial interests or personal relationships that could have appeared to influence the work reported in this paper.

Data availability

The authors do not have permission to share data.

Acknowledgments

The study was supported by the National Key Research and Development Program of China [2018YFC1802002, 2019YFC1804101], National Natural Science Foundation of China [42107405, U1806216], Natural Science Foundation of Tianjin [20JCZDJC00700], and 111 Program, Ministry of Education of China [T2017002].

Appendix A. Supplementary material

Supplementary data associated with this article can be found in the online version at doi:10.1016/j.apcatb.2022.122246.

References

- [1] H. Dong, C. Zhang, J. Deng, Z. Jiang, L. Zhang, Y. Cheng, K. Hou, L. Tang, G. Zeng, Factors influencing degradation of trichloroethylene by sulfide-modified nanoscale zero-valent iron in aqueous solution, *Water Res.* 135 (2018) 1–10.
- [2] A.N. Garcia, Y. Zhang, S. Ghoshal, F. He, D.M. O'Carroll, Recent advances in sulfidated zerovalent iron for contaminant transformation, *Environ. Sci. Technol.* 55 (2021) 8464–8483.
- [3] D. Fan, Y. Lan, P.G. Tratnyek, R.L. Johnson, A. Agrawal, Sulfidation of iron-based materials: a review of processes and implications for water treatment and remediation, *Environ. Sci. Technol.* 51 (2017) 13070–13085.
- [4] C.K. Li, H. Yang, W.J. Chang, X. Feng, S. Liou, Trace key mechanistic features of the arsenite sequestration reaction with nanoscale zerovalent iron, *J. Am. Chem. Soc.* 143 (2021) 16538–16548.
- [5] Z. Cao, J. Xu, H. Li, T. Ma, X. Xu, Dechlorination and defluorination capability of sulfidized nanoscale zerovalent iron with suppressed water reactivity, *Chem. Eng. J.* 400 (2020), 125900.
- [6] F. He, L. Gong, D. Fan, P.G. Tratnyek, G.V. Lowry, Quantifying the efficiency and selectivity of organohalide dechlorination by zerovalent iron, *Environ. Sci. Process. Impacts* 22 (2020) 528–542.
- [7] J. Xu, J. Tang, S.A. Baig, X. Lv, X. Xu, Enhanced dechlorination of 2,4-dichlorophenol by Pd/Fe₃O₄ nanocomposites, *J. Hazard. Mater.* 244–245 (2013) 628–636.
- [8] W. Xu, Z. Li, S. Shi, J. Qi, S. Cai, Y. Yu, D.M. O'Carroll, F. He, Carboxymethyl cellulose stabilized and sulfidated nanoscale zero-valent iron: characterization and trichloroethene dechlorination, *Appl. Catal. B* 262 (2020), 118303.
- [9] J. Xu, X. Liu, Z. Cao, W.L. Bai, Q.Y. Shi, Fast degradation, large capacity, and high electron efficiency of chloramphenicol removal by different carbon-supported nanoscale zerovalent iron, *J. Hazard. Mater.* 384 (2020), 121253–121253.
- [10] H. Li, J. Zhang, K. Gu, J. Li, Sulfidation of zerovalent iron for improving the selectivity toward Cr(VI) in oxalic water: Involvements of FeS_x, *J. Hazard. Mater.* 409 (2020), 124498.
- [11] S. Cai, B. Chen, X. Qiu, J. Li, P.G. Tratnyek, F. He, Sulfidation of zero-valent iron by direct reaction with elemental sulfur in water: efficiencies, mechanism, and dechlorination of trichloroethylene, *Environ. Sci. Technol.* 55 (2021) 645–654.
- [12] H. Qin, X. Guan, J.Z. Bandstra, R.L. Johnson, P.G. Tratnyek, Modeling the kinetics of hydrogen formation by zerovalent iron: effects of sulfidation on micro- and nano-scale particles, *Environ. Sci. Technol.* 52 (2018) 13887–13896.
- [13] D. Fan, G.S.O.B. Johnson, P.G. Tratnyek, R.L. Johnson, Sulfidation of nano zerovalent iron (nZVI) for improved selectivity during in-situ chemical reduction (ISCR), *Environ. Sci. Technol.* 50 (2016) 9558–9565.
- [14] Y. Gu, B. Wang, F. He, M.J. Bradley, P.G. Tratnyek, Mechanochemically sulfidated microscale zero valent iron: pathways, kinetics, mechanism, and efficiency of trichloroethylene dechlorination, *Environ. Sci. Technol.* 51 (2017) 12653–12662.
- [15] L. Gong, X. Qiu, D. Cheng, Y. Hu, Z. Zhang, Q. Yuan, D. Yang, C. Liu, L. Liang, F. He, Coincorporation of N and S into zero-valent iron to enhance TCE dechlorination: kinetics, electron efficiency, and dechlorination capacity, *Environ. Sci. Technol.* 55 (2021) 16088–16098.
- [16] J. Wu, J. Zhao, J. Hou, R.J. Zeng, B. Xing, Degradation of tetrabromobisphenol A by sulfidated nanoscale zerovalent iron in a dynamic two-step anoxic/oxic process, *Environ. Sci. Technol.* 53 (2019) 8105–8114.
- [17] J. Li, X. Zhang, M. Liu, B. Pan, W. Zhang, Z. Shi, X. Guan, Enhanced reactivity and electron selectivity of sulfidated zerovalent iron toward chromate under aerobic conditions, *Environ. Sci. Technol.* 52 (2018) 2988–2997.
- [18] Y. Han, W. Yan, Reductive dechlorination of trichloroethene by zero-valent iron nanoparticles: reactivity enhancement through sulfidation treatment, *Environ. Sci. Technol.* 50 (2016) 12992–13001.
- [19] G.N. Zhou, W.Q. Li, C.S. He, X.C. Liu, R.R. Ding, Y.X. Wang, Y. Mu, Enhanced hydrodeiodination of iodinated contrast medium by sulfide-modified nano-sized zero-valent iron: kinetics, mechanisms and application prospects, *Chem. Eng. J.* 401 (2020), 126050.
- [20] J. Xu, Y. Wang, C. Weng, W. Bai, Y. Jiao, R. Kaegi, G.V. Lowry, Reactivity, selectivity, and long-term performance of sulfidized nanoscale zerovalent iron with different properties, *Environ. Sci. Technol.* 53 (2019) 5936–5945.
- [21] S. Bae, R.N. Collins, T.D. Waite, K. Hanna, Advances in surface passivation of nanoscale zerovalent iron: a critical review, *Environ. Sci. Technol.* 52 (2018) 12010–12025.

- [22] M. Mangayayam, K. Dideriksen, M. Ceccato, D.J. Tobler, The structure of sulfidized zero valent iron by one-pot synthesis: Impact on contaminant selectivity and long-term performance, *Environ. Sci. Technol.* 53 (2019) 4389–4396.
- [23] Z. Cao, H. Li, S. Zhang, Y. Hu, J. Xu, X. Xu, Properties and reactivity of sulfidized nanoscale zero-valent iron prepared with different borohydride amounts, *Environ. Sci. Nano* 8 (2021) 2607–2617.
- [24] Z. Cao, X. Xu, Correlating surface chemistry and hydrophobicity of sulfidized nanoscale zerovalent iron with its reactivity and selectivity for denitration and dechlorination, *Chem. Eng. J.* 394 (2020), 124876.
- [25] J. Xu, A. Avellan, H. Li, X. Liu, G.V. Lowry, Sulfur loading and speciation control the hydrophobicity, electron transfer, reactivity, and selectivity of sulfidized nanoscale zerovalent iron, *Adv. Mater.* 3 (2020), 1906910.
- [26] J. Xu, Z. Cao, H. Zhou, Z. Lou, G.V. Lowry, Sulfur dose and sulfidation time affect reactivity and selectivity of post-sulfidized nanoscale zerovalent iron, *Environ. Sci. Technol.* 53 (2019) 13344–13352.
- [27] M. Zhuang, H. Wang, L. Qi, L. Cui, J. Yan, Production of activated biochar via a self-blowing strategy-supported sulfidated nanoscale zerovalent iron with enhanced reactivity and stability for Cr(VI) reduction, *J. Clean. Prod.* 315 (2021), 128108.
- [28] S. Bhattacharjee, S. Ghoshal, Optimal design of sulfidated nanoscale zerovalent iron for enhanced trichloroethene degradation, *Environ. Sci. Technol.* 52 (2018) 11078–11086.
- [29] P. Huang, P. Zhang, C. Wang, J. Tang, H. Sun, Enhancement of persulfate activation by Fe-biochar composites: synergism of Fe and N-doped biochar, *Appl. Catal. B* 303 (2021), 120926.
- [30] K. Mackenzie, S. Bleyl, A. Georgi, F.D. Kopinke, Carbo-iron-An Fe/AC composite-as alternative to nano-iron for groundwater treatment, *Water Res.* 46 (2012) 3817–3826.
- [31] F. Gao, S. Ahmad, J. Tang, C. Zhang, S. Li, C. Yu, Q. Liu, H. Sun, Enhanced nitrobenzene removal in soil by biochar supported sulfidated nano zerovalent iron: solubilization effect and mechanism, *Sci. Total Environ.* 826 (2022), 153960.
- [32] S. Bleyl, F.D. Kopinke, K. Mackenzie, Carbo-Iron-Synthesis and stabilization of Fe (0)-doped colloidal activated carbon for in situ groundwater treatment, *Chem. Eng. J.* 191 (2012) 588–595.
- [33] S. Wang, M. Zhao, M. Zhou, Y.C. Li, J. Wang, B. Gao, S. Sato, K. Feng, W. Yin, A. D. Igalavithana, P. Oleszczuk, X. Wang, Y.S. Ok, Biochar-supported nZVI (nZVI/BC) for contaminant removal from soil and water: a critical review, *J. Hazard. Mater.* 373 (2019) 820–834.
- [34] T. Sun, B.D.A. Levin, J.J.L. Guzman, A. Enders, D.A. Muller, L.T. Angenent, J. Lehmann, Rapid electron transfer by the carbon matrix in natural pyrogenic carbon, *Nat. Commun.* 8 (2017) 14873.
- [35] J. Liu, J. Jiang, Y. Meng, A. Aihemaiti, X. Chen, Preparation, environmental application and prospect of biochar-supported metal nanoparticles: a review, *J. Hazard. Mater.* 388 (2020), 122026.
- [36] D. Zhang, L. Yang, S. Tong, X. Jiang, L. Wang, X. Sun, J. Li, X. Liu, J. Shen, Biochar supported sulfide-modified nanoscale zero-valent iron for the reduction of nitrobenzene, *RSC Adv.* 8 (2018) 22161–22168.
- [37] H. Li, R. Si, W. Wang, Y. Huang, M. Huang, Sulfidated nanoscale zero-valent iron dispersed in dendritic mesoporous silica nanospheres for degrading tetrabromobisphenol A, *Colloids Surf. A* 621 (2021), 126586.
- [38] D. Li, Z. Mao, Y. Zhong, W. Huang, Y. Wu, P. Peng, Reductive transformation of tetrabromobisphenol A by sulfidated nano zerovalent iron, *Water Res.* 103 (2016) 1–9.
- [39] Y. Li, X. Li, Y. Xiao, C. Wei, W. Huang, Catalytic debromination of tetrabromobisphenol A by Ni/nZVI bimetallic particles, *Chem. Eng. J.* 284 (2016) 1242–1250.
- [40] N. Kang, N. Zhu, W. Guo, C. Shi, P. Wu, X. Wei, Efficient debromination of tetrabromobisphenol A (TBBPA) by Au/Fe@biocarbon derived from bioreduction precious metals, *Chem. Eng. J.* 334 (2018) 99–107.
- [41] Z. Cao, H. Li, G.V. Lowry, X. Shi, J. Xu, Unveiling the role of sulfur in rapid defluorination of florfenicol by sulfidized nanoscale zero-valent iron in water under ambient conditions, *Environ. Sci. Technol.* 55 (2021) 2628–2638.
- [42] H. Wang, Y. Zhong, X. Zhu, D. Li, Y. Deng, W. Huang, P. Peng, Enhanced tetrabromobisphenol A debromination by nanoscale zero valent iron particles sulfidated with S^0 dissolved in ethanol, *Environ. Sci. Process. Impacts* 23 (2021) 86–97.
- [43] J. Xu, A. Avellan, H. Li, E.A. Clark, G. Lowry, Iron and sulfur precursors affect crystalline structure, speciation, and reactivity of sulfidized nanoscale zerovalent iron, *Environ. Sci. Technol.* 54 (2020) 13294–13303.
- [44] Y. Su, A.S. Adeleye, A.A. Keller, Y. Huang, C. Dai, X. Zhou, Y. Zhang, Magnetic sulfide-modified nanoscale zerovalent iron (S-nZVI) for dissolved metal ion removal, *Water Res.* 74 (2015) 47–57.
- [45] S. Song, Y. Su, A.S. Adeleye, Y. Zhang, X. Zhou, Optimal design and characterization of sulfide-modified nanoscale zerovalent iron for diclofenac removal, *Appl. Catal. B* 201 (2017) 211–220.
- [46] Y. Su, A.S. Adeleye, Y. Huang, X. Zhou, A.A. Keller, Y. Zhang, Direct synthesis of novel and reactive sulfide-modified nano iron through nanoparticle seeding for improved cadmium-contaminated water treatment, *Sci. Rep.* 6 (2016) 24358.
- [47] J. Xu, Z. Cao, Y. Wang, Y. Zhang, X. Gao, M.B. Ahmed, J. Zhang, Y. Yang, J.L. Zhou, G.V. Lowry, Distributing sulfidized nanoscale zerovalent iron onto phosphorus-functionalized biochar for enhanced removal of antibiotic florfenicol, *Chem. Eng. J.* 359 (2019) 713–722.
- [48] E. Spielman-Sun, E. Lombi, E. Donner, A. Avellan, B. Etschmann, D. Howard, G. V. Lowry, Temporal evolution of copper distribution and speciation in roots of *Triticum aestivum* exposed to CuO, Cu(OH)₂, and CuS nanoparticles, *Environ. Sci. Technol.* 52 (2018) 9777–9784.
- [49] S. Xiao, Z. Jin, H. Dong, J. Xiao, Y. Li, L. Li, R. Li, J. Chen, R. Tian, Q. Xie, A comparative study on the physicochemical properties, reactivity and long-term performance of sulfidized nanoscale zerovalent iron synthesized with different kinds of sulfur precursors and procedures in simulated groundwater, *Water Res.* 212 (2022), 118097.
- [50] H. Guo, H. Li, K. Jarvis, H. Wan, P. Kunal, S.G. Dunning, Y. Liu, G. Henkelman, S. M. Humphrey, Microwave-assisted synthesis of classically immiscible Ag-Ir alloy nanoparticle catalysts, *ACS Catal.* 8 (2018) 11386–11397.
- [51] L. Ren, L. Li, S. Chen, H. Li, Y. Liu, L. Zhou, S. Guo, Y. Yu, Yolk-shell Fe/FeS@SiO₂ particles with enhanced dispersibility, transportability and degradation of TBBPA, *Catal. Today* 327 (2019) 2–9.
- [52] D. Li, Y. Zhong, H. Wang, W. Huang, P. Peng, Remarkable promotion in particle dispersion and electron transfer capacity of sulfidated nano zerovalent iron by coating alginate polymer, *Sci. Total Environ.* 759 (2020), 143481.
- [53] W. Shen, J. Xu, L. Zhu, Triton X-100 improves the reactivity and selectivity of sulfidized nanoscale zerovalent iron toward tetrabromobisphenol A: implications for groundwater and soil remediation, *J. Hazard. Mater.* 416 (2021), 126119.
- [54] Z. Cao, X. Liu, J. Xu, J. Zhang, Y. Yang, J. Zhou, X. Xu, G.V. Lowry, Removal of antibiotic florfenicol by sulfide-modified nanoscale zero-valent iron, *Environ. Sci. Technol.* 51 (2017) 11269–11277.
- [55] Y. Gu, L. Gong, J. Qi, S. Cai, W. Tu, F. He, Sulfidation mitigates the passivation of zero valent iron at alkaline pHs: experimental evidences and mechanism, *Water Res.* 159 (2019) 233–241.
- [56] G. Yang, H.L. Lee, Chemical reduction of nitrate by nanosized iron: kinetics and pathways, *Water Res.* 39 (2005) 884–894.
- [57] Z. Cui, L. Jian, J. Wu, One-step green preparation of magnetic seaweed biochar/sulfidated Fe0 composite with strengthen adsorptive removal of tetrabromobisphenol A through in situ reduction, *Bioresour. Technol.* 307 (2020), 123170.
- [58] Y. Liu, T. Phenrat, G.V. Lowry, Effect of TCE concentration and dissolved groundwater solutes on NZVI-promoted TCE dechlorination and H₂ evolution, *Environ. Sci. Technol.* 41 (2007) 7881–7887.
- [59] D. Wu, S. Peng, K. Yan, B. Shao, Y. Feng, Y. Zhang, Enhanced As(III) sequestration using sulfide-modified nano-scale zero-valent iron with a characteristic core-shell structure: Sulfidation and As distribution, *ACS Sustain. Chem. Eng.* 6 (2018) 3039–3048.
- [60] Y. Lü, J. Li, Y. Li, L. Liang, H. Dong, K. Chen, C. Yao, Z. Li, J. Li, X. Guan, The roles of pyrite for enhancing reductive removal of nitrobenzene by zero-valent iron, *Appl. Catal. B* 242 (2019) 9–18.
- [61] E.J. Kim, J.H. Kim, A.M. Azad, Y.S. Chang, Facile synthesis and characterization of Fe/FeS nanoparticles for environmental applications, *ACS Appl. Mater. Interfaces* 3 (2011) 1457–1462.
- [62] B. Van Zeghbroeck, Principles of Semiconductor Devices, The Oxford Series in Electrical and Computer Engineering, University of Colorado, 2011.
- [63] R. Dalven, Empirical relation between energy gap and lattice constant in cubic semiconductors, *Phys. Rev. B* 8 (1973) 6033–6034.
- [64] D. Zhang, Y. Li, A. Sun, S. Tong, G. Su, X. Jiang, J. Li, W. Han, X. Sun, L. Wang, Enhanced nitrobenzene reduction by modified biochar supported sulfidated nano zerovalent iron: comparison of surface modification methods, *Sci. Total Environ.* 694 (2019), 133701.
- [65] J. Xu, H. Li, G.V. Lowry, Sulfidized nanoscale zero-valent iron: tuning the properties of this complex material for efficient groundwater remediation, *Acc. Mater. Res.* 2 (2021) 420–431.
- [66] D. Li, X. Zhu, Y. Zhong, W. Huang, P. Peng, Abiotic transformation of hexabromocyclododecane by sulfidated nanoscale zerovalent iron: kinetics, mechanism and influencing factors, *Water Res.* 121 (2017) 140–149.
- [67] P. Fan, Y. Sun, B. Zhou, X. Guan, Coupled effect of sulfidation and ferrous dosing on selenate removal by zerovalent iron under aerobic conditions, *Environ. Sci. Technol.* 53 (2019) 14577–14585.
- [68] Y. Liu, S.A. Majetich, R.D. Tilton, D.S. Sholl, G.V. Lowry, TCE dechlorination rates, pathways, and efficiency of nanoscale iron particles with different properties, *Environ. Sci. Technol.* 39 (2005) 1338–1345.
- [69] D. Cwiertny, S. Bransfield, K. Livi, D. Fairbrother, A. Roberts, Exploring the influence of granular iron additives on 1,1,1-trichloroethane reduction, *Environ. Sci. Technol.* 40 (2006) 6837–6843.
- [70] Y. Xie, D.M. Cwiertny, Chlorinated solvent transformation by palladized zerovalent iron: mechanistic insights from reductant loading studies and solvent kinetic isotope effects, *Environ. Sci. Technol.* 47 (2013) 7940–7948.
- [71] X. Guan, X. Du, M. Liu, H. Qin, J. Qiao, Y. Sun, Enhanced trichloroethylene dechlorination by carbon-modified zero-valent iron: revisiting the role of carbon additives, *J. Hazard. Mater.* 394 (2020), 122564.
- [72] H. Lyu, J. Tang, Y. Huang, L. Gai, E.Y. Zeng, K. Liber, Y. Gong, Removal of hexavalent chromium from aqueous solutions by a novel biochar supported nanoscale iron sulfide composite, *Chem. Eng. J.* 322 (2017) 516–524.
- [73] L. Xie, C. Shang, The effects of operational parameters and common anions on the reactivity of zero-valent iron in bromate reduction, *Chemosphere* 66 (2007) 1652–1659.